Wideband Open-Ended Ridge Gap Waveguide Antenna Elements for 1-D and 2-D Wide-Angle Scanning Phased Arrays at 100 GHz

Citation for the original published paper (version of record):
Zhang, Y., Vilenskiy, A., Ivashina, M. (2022). Wideband Open-Ended Ridge Gap Waveguide Antenna Elements for 1-D and 2-D Wide-Angle Scanning
Phased Arrays at 100 GHz. IEEE Antennas and Wireless Propagation Letters.
http://dx.doi.org/10.1109/LAWP.2022.3150595

Wideband Open-Ended Ridge Gap Waveguide Antenna Elements for 1-D and 2-D Wide-Angle Scanning Phased Arrays at 100 GHz

Yingqi Zhang, *Student member, IEEE,* Artem R. Vilenskiy, *Member, IEEE,* and Marianna V. Ivashina, *Senior Member, IEEE*

***Abstract*—A new antenna element type based on the open-ended ridge gap waveguide (RGW) is proposed for phased array applications. This element type is of a particular interest at high mm-wave frequencies ($\geq$ 100 GHz) owing to a contactless design alleviating active beam-steering electronics integration. The key challenge addressed here is a realization of a wide fractional bandwidth and scan range with high radiation efficiency. We demonstrate a relatively simple wideband impedance matching network comprised of an aperture stepped ridge segment and a single-pin RGW section. Furthermore, the E- and H-plane grooves are added that effectively suppress antenna elements mutual coupling. Results demonstrate a wide-angle beam steering ($\geq$ 50°) over $\geq$ 20% fractional bandwidth at W-band with $\geq$ 89% radiation efficiency that significantly outperforms existing solutions at these frequencies. An experimental prototype of a 1×19 W-band array validates the proposed design concept through the embedded element pattern measurements.**

***Index Terms*—mm-wave antenna, array antenna, wideband array, ridge gap waveguide, wide-angle beam steering.**

I. Introduction

THE future wireless communication beyond 5G holds the promise to reach Tbps level throughput at distances $\geq$ 1 km with flexible user mobility [1]. The upper millimeter-wave (mm-wave) bands (100+ GHz), especially W- and D-band, are being widely considered for these applications, owing to the wide available bandwidth, a relatively low atmospheric attenuation, and cm-level positioning accuracy [2]. In this context, high-gain mm-wave antenna systems with intelligent beamforming are seen as the key technological enablers, capable to compensate the considerable free-space path loss at these frequencies, while supporting spatial multiplexing, and users tracking. This drives the research in 100+ GHz phased array antennas with electronic beam steering that can provide a broad coverage and high energy efficiency [3].

A popular choice of W/D-band array antennas employs Antenna-on-Chip (AoC) and Antenna-in-Package (AiP) technologies which have been realized using quartz substrates [4] or multilayer packages [5], [6]. However, these designs exhibit a relatively narrow bandwidth ($\leq$ 10%) and low radiation efficiency ($\leq$ 40%), along with a limited beam-steering range ($\leq$ 30°), mainly due to high material loss and surface wave effects. An alternative approach is 3-D antenna configurations, using quasi-optical structures (e.g., Luneburg lens [7]) to extend the coverage, at the cost of a bulky design. Another wideband solution is dielectric rod arrays with liquid crystal-based phase control [8]; its drawback is a relatively small beam-steering range and complicated assembly.

Manuscript received xx xx, 2021; revised xx xx, 2021. This work has received funding from the EU Horizon 2020 research, innovation programme under the MCA grant agreement No. 860023, and Swedish Foundation for Strategic Research STP19-0043. *(Corresponding author: Y. Zhang)*

The authors are with the Electrical Engineering Department, Chalmers University of Technology, Gothenburg 41258, Sweden (e-mail: yingqi@chalmers.se).

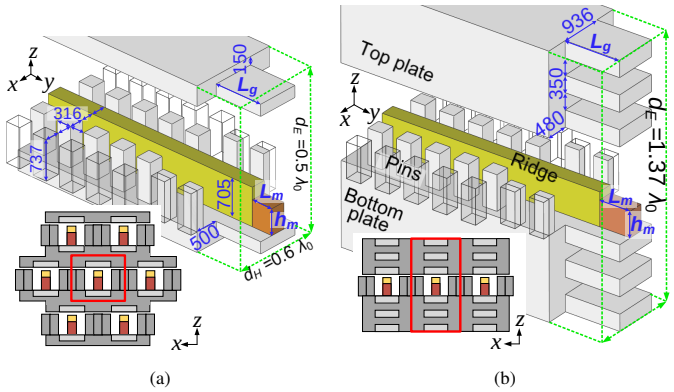

Fig. 1. The proposed open-ended RGW element designs for (a) 2-D array (isosceles triangular grid) and (b) 1-D array. The components of the adjacent elements in the H-plane are shown semi-transparent (unit: μm).

More recently, full-metal planar array antenna designs have been investigated at W- and D-band [9]–[14]. Realization of electronic beam steering in this case is considerably more challenging than for AoC, AiP, and lens arrays. The reason is too small physical space available to integrate phase-shifting circuitry in each array element at such high frequencies. As the result, most reported arrays have been designed for fixed-beam scenarios, or as frequency beam-steering arrays [13], [14].

Therefore, we propose a new antenna element type based on the open-ended ridge gap waveguide (RGW) that aims to overcome the above-mentioned limitations. The starting point of this design is a traditional ridge waveguide (WG) element which has been widely used in arrays at microwave frequencies [15], [16]. However, at high mm-wave frequencies, these hollow metal designs are rare due to the increased manufacturing complexity and the above-explained difficulties of electronics integration. On the other hand, the relatively new gap waveguide technology [17], realizing contactless WGs in a bed of nails, can be effectively utilized to resolve these problems. The concept of such an element has been introduced in [18], albeit without a design optimization strategy and no practical implementation considerations. The present work fills

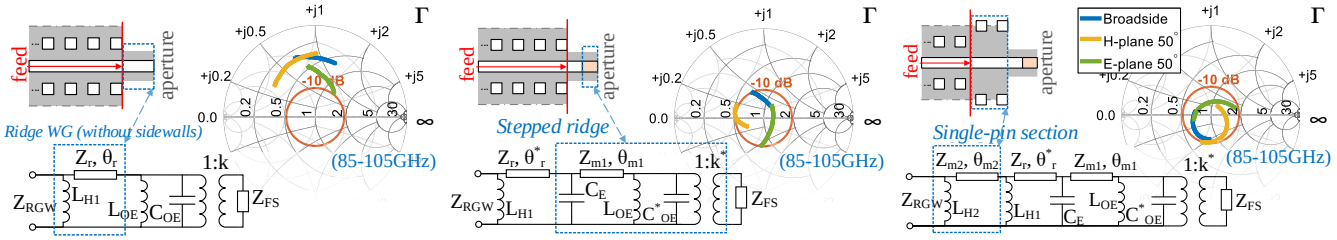

(a) No matching circuit (b) Stepped ridge segment (c) Stepped ridge + single-pin section

Fig. 2. Impedance matching mechanism of the RGW element, represented by equivalent circuits. Open-ended RGW aperture parameters (beam steering-dependent): Z_{FS} is the free-space impedance, $k^{(*)}$, $C_{OE}^{(*)}$, and L_{OE} are the equivalent transformer turn ratio, capacitance, and inductance with (*) and without the stepped ridge, respectively. Matching circuit parameters: $(Z_r, \theta_r^{(*)})$, (Z_{m1}, θ_{m1}), and (Z_{m2}, θ_{m2}) are the characteristic impedance and electrical length of the output ridge WG, stepped ridge, and single-pin segments; C_E and $L_{H1,2}$ are the equivalent capacitance and inductance of the E-plane ridge and H-plane pin sidewalls steps.

in this knowledge gap by providing a detailed element design and its experimental demonstration. This results in two W-band element examples, one of which can be used in 1-D linear arrays and another in 2-D arrays (Fig. 1), both with competitive performance characteristics in terms of high efficiency over a wide scan range and wide bandwidth.

II. Open-Ended RGW Array Elements: Design and Beam-Steering Performance

In this research, all array elements are based on a regular RGW [19] as depicted in Fig. 1. The RGW employs a single ridge with two rows of pins on each side. The following main design dimension are used: ridge height 705 μm, width 316 μm; pins height 737 μm, width 316 μm; the gap between the pins and the separation between the pins and the ridge is 316 μm; the air gap between the ridge and the top metal plate is 137 μm. Thus, the element H-plane (xy-plane, Fig. 1) size $d_H = 0.6\lambda_0 = 1896$ μm, where λ_0 is the free-space wavelength at the central design frequency $f_0 = 95$ GHz. A single quasi-TEM mode operation regime spans the $80 - 160$ GHz band. Design material is aluminum. In all simulations, the 0.5-μm Groisse surface roughness model is used. A detailed characterization of this RGW can be found in [20].

A. 2-D Array RGW Element

A design of the proposed RGW element for a 2-D array is detailed in Fig. 1(a). As seen, the basic RGW is terminated in the open-ended manner that couples the propagating RGW wave to free space. A structure comprised of a stepped ridge segment (length L_m and height h_m) and a single-pin RGW section realizes a broadband impedance match and is discussed below. In the H-plane, multiple array elements are manufactured on a common metal plate being separated by the pins. By stacking such sub-arrays in the E-plane (yz-plane) the full 2-D array is constructed. Active beam-steering electronics can be integrated in a top metal plate of each RGW and contactlessly coupled to the ridge employing an E-plane WG bifurcation [21]. That creates an important design advantage of such element at high mm-wave frequencies. The considered 2-D array elements are arranged in an isosceles triangular lattice. The E-plane element size is $d_E = 0.5\lambda_0 = 1576$ μm.

The full-wave element model was built in Ansys HFSS using the 2-D infinite array approach with sidewalls periodic

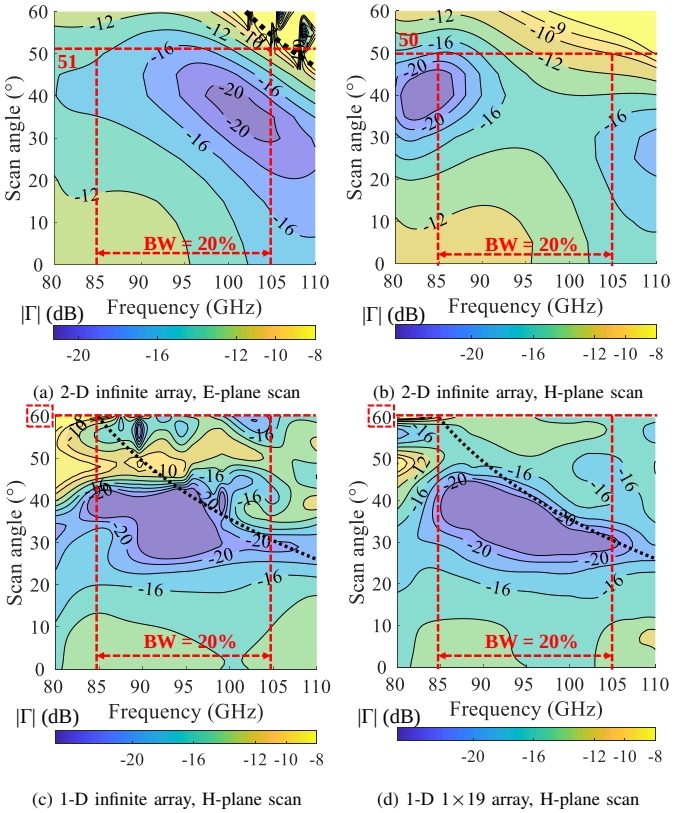

(a) 2-D infinite array, E-plane scan (b) 2-D infinite array, H-plane scan

(c) 1-D infinite array, H-plane scan (d) 1-D 1×19 array, H-plane scan

Fig. 3. Simulated active reflection coefficient (Γ) maps for the RGW element of the 2-D infinite, 1-D infinite, and 1-D finite (1×19) arrays.

boundary conditions (PBC) and a Floquet port at 10-mm distance above the aperture. Compared with the initial design presented in [18], the RGW element has been further modified in this study. Apart from E-plane grooves used above and below the ridge [Fig.1(a)], H-plane grooves have been formed by removing the metal on both sides of the ridge. The resulting width of the E- and H-plane grooves is 300 μm and 1000 μm, respectively, while the depth is L_g. This way, the output RGW section transforms into the ridge WG without sidewalls. As shown below, this measure further reduced the H-plane elements mutual coupling.

The element's design parameters L_m, h_m, and L_g have been optimized to achieve a maximum scanning range in the 20% relative bandwidth (85–105 GHz), as defined by the active reflection coefficient $|\Gamma| \leq -10$ dB criterion. Fig. 2 consis-

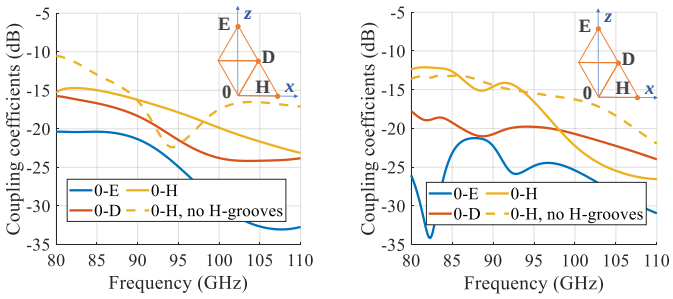

(a) (b)

Fig. 4. Mutual coupling levels between the central ("0") and adjacent elements in E-/D-/H-planes in (a) RGW array; (b) ridge WG array [18].

tently explains the impedance matching mechanism utilizing a simplified equivalent circuit representation:

1) As seen in Fig. 2(a), the open-ended ridge WG fails to achieve a good impedance match. This is largely due to an excessive shunting edge capacitance of the ridge C_{OE}.
2) The high-impedance (Z_{m1}) stepped ridge segment [Fig. 2(b)] realizes (i) a C_{OE} reduction to C^*_{OE} and (ii) an impedance transformation, while adding an equivalent E-plane ridge step capacitance C_E. As a result, Γ curves are effectively shifted to the center of the Smith chart.
3) Finally, the low-impedance (Z_{m2}) single-pin section [Fig. 2(c)] locates all Γ curves well inside the -10-dB circle by providing a fine impedance transformation and adding an inductance L_{H2} of the H-plane sidewalls step.

The final optimized design parameters are $L_m = 466$ μm, $h_m = 480$ μm, $L_g = 1060$ μm. The resulting beam-steering performance is demonstrated in Figs. 3(a), 3(b). For the 20% bandwidth the beam-steering range is $\pm 51^\circ$ and $\pm 50^\circ$ in the E-and H-plane, respectively. In the E-plane, at higher-frequencies, the scan range is limited by the grating-lobe border (black dashed curves in Fig. 3). Here, the element also experiences the scan blindness. On the other hand, in the H-plane, we observe no scan blindness in contrast to the RGW element design from [18]. The elimination of this phenomenon is attributed to the E- and H-plane grooves that effectively create an aperture quasi-periodic electromagnetic soft surface [22] [see the inset in Fig. 1(a)]. Fig. 4 demonstrates realized mutual coupling levels between the central and three adjacent elements for the proposed and ridge WG array from [18]. Both arrays show quite similar coupling performance that proves the similarity of electromagnetic processes in the open-ended elements. For comparison, simulated results in the H-plane are also given for the elements without H-plane grooves (dashed curves). For the grooved designs, we observe the expected high-frequency H-plane mutual coupling suppression by up to 7 dB, which greatly improves the scan range. Inside the beam-steering range, the simulated element radiation efficiency is $> 95\%$; the relative cross-polarization level is below -60 dB and -17 dB in the E- and H-plane, respectively.

B. 1-D Array RGW Element

A linear array design is of practical interest as a building block (sub-array) of the 2-D array antenna. Furthermore, mm-wave 1-D beam-steering arrays have found their application for the indoor communication [23] and automotive radar systems [24]. In these cases, the proposed open-ended RGW element concept can be readily utilized. The 1-D element structure is detailed in Fig. 1(b). As seen, the design has been, in general, inherited from the 2-D array element. The main discrepancy is the two-groove structure formed in the E-plane. The resulting aperture electromagnetic soft surface [see the inset in Fig. 1(b)] allows to predictably terminate and stop the leakage of electrical currents to the outer surfaces of the top and bottom metal plates. To be consistent with the previous 2-D array element design, we have used $d_H = 0.6\lambda_0$.

Again, the 1-D element design has been optimized with the maximum scan range criterion (Section II-A). A full-wave HFSS simulation model with the H-plane PBC and perfect matched layers (along y- and z-axis) has been employed for this purpose. The final design parameters are $L_m = 676$ μm, $h_m = 539$ μm, $L_g = 1200$ μm. The simulated $|\Gamma|$ map is presented in Fig. 3(c). The 1-D element demonstrates a wideband impedance matching performance with $|\Gamma| \leq -10$ dB. The grating-lobe border limits the scan range for some applications. However, this can be easily compensated by decreasing d_H.

III. Experimental Study of the 1-D Array Element

At this research stage, the first prototype of the 1-D array has been designed for the experimental characterization to verify the predicted RGW element scan performance, as well as to test a manufacturing technology and assembling tolerances. The 1×19 1-D array (Fig. 5) has been fabricated using a CNC milling process. This array size was found sufficient to reconstruct the infinite array environment as supported by results in Fig. 3(d) demonstrating simulated $|\Gamma|$ of the central array element [*cf.* Fig. 3(c)]. Since the standard WR-10 interface flange is much larger than d_H, measuring the full array S-matrix (to compute Γ) is practically not possible. Therefore, the beam-steering performance of the element was characterized through embedded element pattern (EEP) measurements [25]. To realize this, the central array element was excited using a WR10-to-RGW orthogonal transition [17] [Fig. 5(a)], while all neighboring elements were terminated with matched loads. The loads were made of carbon-loaded absorbing foam (ABS) WAVASORB FS from Emerson & Cuming [20].

Element performance was measured at the WR-10 input flange in the compact antenna test range (CATR) setup of Chalmers THz antenna chamber [Fig. 5(b)]. The measured central element passive reflection coefficient (S_{11}) and the

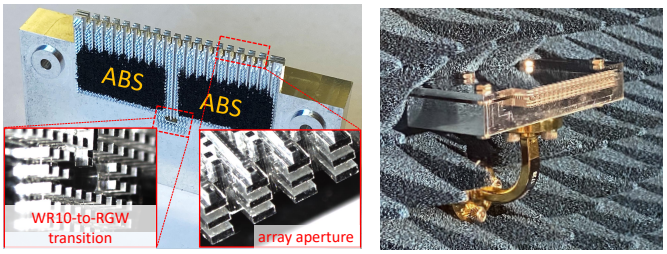

(a) (b)

Fig. 5. (a) Photograph of the manufactured 1-D open-ended RGW array (top plate removed) and (b) the antenna in the CATR measurement setup.

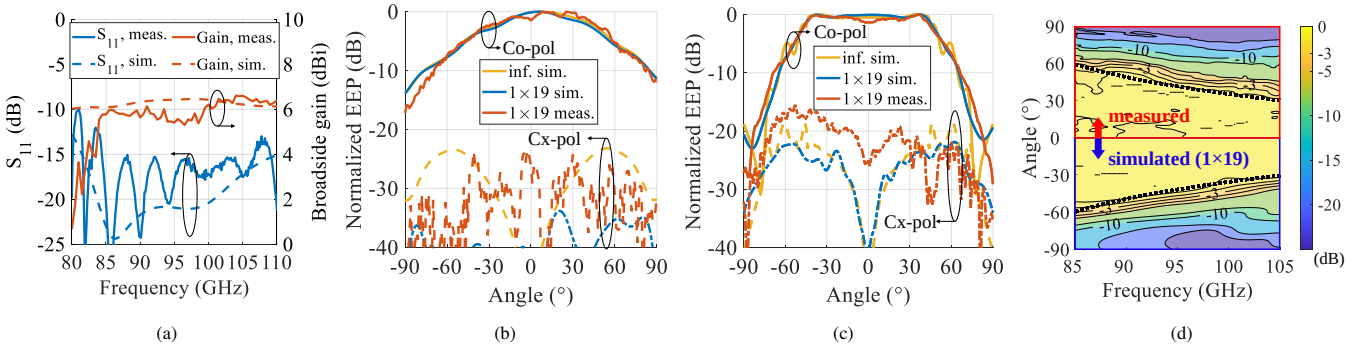

Fig. 6. Simulated and measured performance of the 1-D array RGW element: (a) reflection coefficient (S_{11}) and broadside realized gain; (b) E-plane and (c) H-plane normalized embedded element patterns (EEPs) at 95 GHz; (d) H-plane co-polarized frequency-angle 2-D EEP maps (the dashed black lines indicate the grating-lobe border).

TABLE I
PERFORMANCE COMPARISON OF REPORTED ARRAY ELEMENTS AT HIGH MM-WAVE FREQUENCY BANDS.

Array element type		Implementation technology	Freq. range (GHz) ($\|\Gamma\| \leq$–10 dB)	Element size (λ_0^2)	Radiation efficiency (%)	Scan range / scan loss
[6]	Planar stacked patch	AiP	88-94, 7%	0.49×0.49	N/A	±32° (E/H-plane) / NA
[4]	Planar dif.-fed dipole	AoC (quartz)	108-114, 5%	0.5×0.5	45	±30° (E/H-plane) / ≤ 2.5 dB
[13]	Leaky-wave slot WG	Si micromachining (gold)	220-300, 30%	0.49×0.35	79 (full antenna)	–75° to –30° (E-plane) / NA
[8]	Dielectric rod	Milled Rexolite assembly	75-110, 38%	0.86×0.86	N/A	–25° to 15° (E-plane, 85 GHz) / ≤2.5 dB
This work	Open-ended RGW: **1-D**	Full-metal (aluminum), contactless	85-105, 21%	1.37×0.6	≥ 91	±40° (H-plane) / ≤ 3 dB
	2-D		85-105, 21%	0.5×0.6	≥ 89	±51°/±50° (E/H-plane) / ≤2.5 dB

broadside realized element gain are given in Fig. 6(a) in comparison with the simulated curves. An additional insertion loss (∼0.7 dB) of the WR10-to-RGW transition and an RGW feed line has been extracted from back-to-back structure measurements and excluded from the measured gain results. Some frequency ripples are observed for both S_{11} and gain measured curves. The ripples are attributed to relatively high manufacturing errors ($\leq$ 20 μm) of the stepped ridge height in the transition and aperture areas. Moreover, the realized gain is affected by imperfect ABS loads performance (average reflection coefficient ∼17 dB [20]). The experimental embedded element radiation efficiency was estimated to be $\geq$ 91%, considering simulated values of $\geq$ 97% and an average measured gain loss of 0.3 dB. Simulated (for both the 1×19 array and the 1-D infinite array model) and measured normalized EEPs at 95 GHz are compared in Figs. 6(b), 6(c) for the E- and H-plane, respectively. A small (∼1 dB) H-plane broadside dip, observed for the measured pattern, is due to the above-mentioned non-zero reflections in the ABS-terminated channels. The measured cross-polarized EEP is slightly asymmetrical that is, likely, attributed to the measurement setup. Fig. 6(d) depicts the frequency-angle 2-D co-polarized EEP maps in the H-plane revealing a wide-angle flat-top EEP shape. Array edge effects have been studied in simulations, from which we can conclude that already for the second edge element the EEP shape in the ±50° range deviates by less than 2 dB from the results in Fig. 6. Overall, simulated and measured results in the 85 – 105 GHz range are in a very good agreement, verifying the expected wideband and wide-angle RGW element beam-steering performance with low sensitivity to manufacturing and assembling tolerances.

Table I summarizes the beam-steering performance of the previously reported mm-wave (100+ GHz) array elements implemented in different technologies. The proposed designs outperform the state-of-the-art W- and D-band antenna solutions based on AoC, AiP, and dielectric rod arrays [4]–[6], [8], as well as leaky-wave metal antennas [13], [14] in terms of wide-angle, wideband beam-steering capabilities with high radiation efficiency. The demonstrated 2-D array element performance has been, thus far, achieved for the open-ended ridge WG elements [15] and rectangular WG elements [26] only at much lower frequency bands (L- and X-band), employing impedance-matching dielectric sheets and WG insets.

IV. Conclusions and Future Work

In this letter, we have proposed the open-ended ridge gap waveguide (RGW) antenna element concept for 1- and 2-D array configurations. This RGW element is easily manufacturable from two split blocks which can be thereafter assembled contactlessly. The latter provides that the element is suitable for the integration of active electronics inside its structure to enable electronic beam steering at high mm-wave frequencies. The results of the infinite array simulation model have been verified through the experimental study of the 1-D array element. At W-band, the 2-D array element demonstrates a wideband ($\geq$ 20%) and wide-angle ($\geq$ 50°) beam-steering performance with high radiation efficiency ($\geq$ 89%, with 0.3 dB additional loss included). The future work aims at the development of a 2-D array prototype as well as at integration of phase-shifting circuitry into the element's RGW. A quasi-optical feed architecture [27] is being considered for efficient array elements excitation.

REFERENCES

[1] "European vision for the 6G network ecosystem," White Paper, The 5G Infrastructure Association, Jun. 2021.

[2] T. S. Rappaport, Y. Xing, O. Kanhere, S. Ju, A. Madanayake, S. Mandal, A. Alkhateeb, and G. C. Trichopoulos, "Wireless communications and applications above 100 GHz: Opportunities and challenges for 6G and beyond," *IEEE Access*, no. 7, pp. 78 729–78 757, 2019.

[3] M. V. Ivashina, A. R. Vilenskiy, H.-T. Chou, J. Oberhammer, and M. Ng Mou Kehn, "Antenna technologies for beyond-5G wireless communication: Challenges and opportunities," in *Proc. 2021 International Symposium on Antennas and Propagation (ISAP)*, Taipei, Taiwan, 2021, pp. 1–2.

[4] W. Shin, B.-H. Ku, O. Inac, Y.-C. Ou, and G. M. Rebeiz, "A 108–114 GHz 4× 4 wafer-scale phased array transmitter with high-efficiency on-chip antennas," *IEEE Journal of Solid-State Circuits*, vol. 48, no. 9, pp. 2041–2055, 2013.

[5] S. Shahramian, M. J. Holyoak, A. Singh, and Y. Baeyens, "A fully integrated 384-element, 16-tile, W-band phased array with self-alignment and self-test," *IEEE Journal of Solid-state Circuits*, vol. 54, no. 9, pp. 2419–2434, 2019.

[6] X. Gu, D. Liu, C. Baks, J.-O. Plouchart, W. Lee, and A. Valdes-Garcia, "An enhanced 64-element dual-polarization antenna array package for W-band communication and imaging applications," in *Proc. 2018 IEEE 68th Electronic Components and Technology Conference (ECTC)*, 2018, pp. 197–201.

[7] S. Manafi, J. F. González, and D. Filipovic, "Design of a perforated flat luneburg lens antenna array for wideband millimeter-wave applications," in *Proc. 2019 13th European Conference on Antennas and Propagation (EuCAP)*, 2019, pp. 1–5.

[8] R. Reese, E. Polat, H. Tesmer, J. Strobl, C. Schuster, M. Nickel, A. B. Granja, R. Jakoby, and H. Maune, "Liquid crystal based dielectric waveguide phase shifters for phased arrays at W-band," *IEEE Access*, vol. 7, pp. 127 032–127 041, 2019.

[9] B. L. Cannon, K. J. Vanhille, and G. A. Sadowy, "Microfabricated dual-polarized, W-band antenna architecture for scalable line arrav feed," in *2015 IEEE International Symposium on Antennas and Propagation & USNC/URSI National Radio Science Meeting*, 2015, pp. 615–616.

[10] S. S. Yao and Y. J. Cheng, "W-band high-efficiency wideband planar array antenna based on mems micromachining technology," in *Proc. 2018 48th European Microwave Conference (EuMC)*, 2018, pp. 942–945.

[11] D. Kim, J. Hirokawa, M. Ando, J. Takeuchi, and A. Hirata, "64×64-element and 32×32-element slot array antennas using double-layer hollow-waveguide corporate-feed in the 120 GHz band," *IEEE Trans. Antennas Propag.*, vol. 62, no. 3, pp. 1507–1512, 2014.

[12] J. W. Jordan, S. Lynch, M. Clark, B. L. Cannon, L. A. Adames, D. Wrenn, K. Jackson, N. Erickson, J. Clough, D. Brown *et al.*, "Monolithically fabricated 4096-element, polystrata® broadband d-band array demonstrator," in *Proc. 2019 IEEE MTT-S International Microwave Symposium (IMS)*, 2019, pp. 1060–1063.

[13] A. Gomez-Torrent, M. Garcia-Vigueras, L. Le Coq, A. Mahmoud, M. Ettorre, R. Sauleau, and J. Oberhammer, "A low-profile and high-gain frequency beam steering subterahertz antenna enabled by silicon micromachining," *IEEE Trans. Antennas Propag.*, vol. 68, no. 2, pp. 672–682, 2020.

[14] D. A. Schneider, M. Rösch, A. Tessmann, and T. Zwick, "A low-loss W-band frequency-scanning antenna for wideband multichannel radar applications," *IEEE Antennas and Wireless Propagation Letters*, vol. 18, no. 4, pp. 806–810, 2019.

[15] J. Montgomery, "Ridged waveguide phased array elements," *IEEE Trans. Antennas Propag.*, vol. AP-24, no. 1, pp. 46–53, 1976.

[16] A. Agrawal, M. Perry, and N. Landry, "Wideband ridge waveguide radiating element for phased array antennas," in *Proc. IEEE Antennas and Propagation Society International Symposium. 1995 Digest*, vol. 1, 1995, pp. 568–571.

[17] A. U. Zaman and P.-S. Kidal, *Gap Waveguide in Handbook of Antenna Technologies*. New York, NY: Springer Science+ Business Media Singapore, 2015, p. 464.

[18] Y. Zhang, A. R. Vilenskiy, and M. V. Ivashina, "W-band waveguide antenna elements for wideband and wide-scan array antenna applications for beyond 5G," in *Proc. 2021 15th European Conference on Antennas and Propagation (EuCAP)*, 2021, pp. 1–5.

[19] P.-S. Kildal, E. Alfonso, A. Valero-Nogueira, and E. Rajo-Iglesias, "Local metamaterial-based waveguides in gaps between parallel metal plates," *IEEE Antennas Wireless Propag. Lett.*, vol. 8, pp. 84–87, 2009.

[20] A. R. Vilenskiy, Y. Zhang, and M. V. Ivashina, "Methods for attenuating and terminating waves in ridge gap waveguide at W-band: Carbon-loaded foam, carbonyl iron paint, and nickel plating," in *Proc. 51 European Microwave Conference (EuMC)*, 2021, pp. 1–5, accepted.

[21] A. Aljarosha, A. U. Zaman, and R. Maaskant, "A wideband contactless and bondwire-free mmic to waveguide transition," *IEEE Microwave and Wireless Components Letters*, vol. 27, no. 5, pp. 437–439, 2017.

[22] P.-S. Kildal, "Definition of artificially soft and hard surfaces for electromagnetic waves," *Electronics Letters*, vol. 24, p. 168 – 170, Feb. 1988.

[23] W. Hong, K.-H. Baek, Y. Lee, Y. Kim, and S.-T. Ko, "Study and prototyping of practically large-scale mmWave antenna systems for 5G cellular devices," *IEEE Communications Magazine*, vol. 52, no. 9, pp. 63–69, 2014.

[24] U. Chipengo, A. Sligar, and S. Carpenter, "High fidelity physics simulation of 128 channel mimo sensor for 77 GHz automotive radar," *IEEE Access*, vol. 8, pp. 160 643–160 652, 2020.

[25] N. Amitay, V. Galindo, and C. P. Wu, *Theory and Analysis of Phased Array Antennas*. New York: Wiley Interscience, 1972.

[26] X. Liang, Z. Zhang, J. Zeng, F. Guan, X. Liu, and J. Zi, "Scan blindness free design of wideband wide-scanning open-ended waveguide phased array," *IEEE Access*, vol. 9, pp. 68 127–68 138, 2021.

[27] A. R. Vilenskiy, E. Galesloot, Y. Zhang, A. Bart Smolders, and M. V. Ivashina, "Quasi-optical beamforming network for millimeter-wave electronically scanned array antennas with 1-bit phase resolution," in *Proc. 2021 15th European Conference on Antennas and Propagation (EuCAP)*, 2021, pp. 1–5.